AWARD NUMBER:    W81XWH-12-2-0075


TITLE:   Lifetime Fluorescence and Raman Imaging for Detection of Wound Failure and Heterotopic Ossification


PRINCIPAL INVESTIGATOR:   Dr. Warren Grundfest


CONTRACTING ORGANIZATION:  Regents of the University of California
Los Angeles, CA 90095


REPORT DATE: December 2015


TYPE OF REPORT:   Final


PREPARED FOR:     U.S. Army Medical Research and Materiel Command
                            Fort Detrick, Maryland  21702-5012


DISTRIBUTION STATEMENT: Approved for Public Release; Distribution Unlimited


The views, opinions and/or findings contained in this report are those of the author(s) and should not be construed as an official Department of the Army position, policy or decision unless so designated by other documentation.

# REPORT DOCUMENTATION PAGE

Public reporting burden for this collection of information is estimated to average 1 hour per response, including the time for reviewing instructions, searching existing data sources, gathering and maintaining the data needed, and completing and reviewing this collection of information. Send comments regarding this burden estimate or any other aspect of this collection of information, including suggestions for reducing this burden to Department of Defense, Washington Headquarters Services, Directorate for Information Operations and Reports (0704-0188), 1215 Jefferson Davis Highway, Suite 1204, Arlington, VA 22202-4302. Respondents should be aware that notwithstanding any other provision of law, no person shall be subject to any penalty for failing to comply with a collection of information if it does not display a currently valid OMB control number. **PLEASE DO NOT RETURN YOUR FORM TO THE ABOVE ADDRESS.**

| 1. REPORT DATE | 2. REPORT TYPE | 3. DATES COVERED |
|---|---|---|
| December 2015 | Final | 15Sep2012 - 14Sep2015 |

**4. TITLE AND SUBTITLE**

Lifetime Fluorescence and Raman Imaging for Detection of Wound Failure and Heterotopic Ossification

**5a. CONTRACT NUMBER**
W81XWH-12-2-0075

**5b. GRANT NUMBER**

**5c. PROGRAM ELEMENT NUMBER**

**6. AUTHOR(S)**

Dr. Warren Grundfest

**5d. PROJECT NUMBER**

**5e. TASK NUMBER**

**5f. WORK UNIT NUMBER**

E-Mail: warrenbe@seas.ucla.edu

**7. PERFORMING ORGANIZATION NAME(S) AND ADDRESS(ES)**

Regents of the University of California
Los Angeles, CA 90095

**8. PERFORMING ORGANIZATION REPORT NUMBER**

**9. SPONSORING / MONITORING AGENCY NAME(S) AND ADDRESS(ES)**

U.S. Army Medical Research and Materiel Command
Fort Detrick, Maryland 21702-5012

**10. SPONSOR/MONITOR'S ACRONYM(S)**

**11. SPONSOR/MONITOR'S REPORT NUMBER(S)**

**12. DISTRIBUTION / AVAILABILITY STATEMENT**

Approved for Public Release; Distribution Unlimited

**13. SUPPLEMENTARY NOTES**

**14. ABSTRACT**

The aim of this effort was to develop Raman and lifetime fluorescence imaging systems to assess failed wounds. The goal of these studies was to develop novel contrast mechanisms based on tissue pathologies which allow surgeons to identify wounds at risk for failure based on classifiers identified with these imaging systems. Our collaborative team built and characterized novel video rate imaging systems based on these technologies as a first step towards enabling early and accurate detection of failed wounds. Soldiers wounded in combat present with acute, traumatic wounds resulting from blasts, high speed projectiles, or intense burns. These injuries exhibit complicated healing responses and often fail to heal despite the application of advanced treatments [1-3]. Long term failure facilitates increased risk of infection and can lead to permanent disabilities or death. Current treatment methods include regular debridement of wounds, prophylactic antibiotics, special dressings, and wound drainage systems [1, 4]. Histopathologic testing of excised tissue from wounds for abnormal collagens, inflammatory cytokines, and phosphates have provided insight into the pathophysiology of wounds [1, 5, 6]. However, these are research techniques and due to their expense cannot be done with sufficient frequency to predict wound failure. We hypothesize that systems based on Raman and lifetime fluorescence imaging can give early warning of possible wound failure and provide additional information that will refine the treatment plan and improve wound healing prognoses.

**15. SUBJECT TERMS**

None listed

| 16. SECURITY CLASSIFICATION OF: | | | 17. LIMITATION OF ABSTRACT | 18. NUMBER OF PAGES | 19a. NAME OF RESPONSIBLE PERSON USAMRMC |
|---|---|---|---|---|---|
| a. REPORT | b. ABSTRACT | c. THIS PAGE | Unclassified | 22 | 19b. TELEPHONE NUMBER (include area code) |
| Unclassified | Unclassified | Unclassified | | | |

# Table of Contents

1. **INTRODUCTION:**

    The aim of this effort was to develop Raman and lifetime fluorescence imaging systems to assess failed wounds. The goal of these studies was to develop novel contrast mechanisms based on tissue pathologies which allow surgeons to identify wounds at risk for failure based on classifiers identified with these imaging systems. Our collaborative team built and characterized novel video rate imaging systems based on these technologies as a first step towards enabling early and accurate detection of failed wounds.

    Soldiers wounded in combat present with acute, traumatic wounds resulting from blasts, high speed projectiles, or intense burns. These injuries exhibit complicated healing responses and often fail to heal despite the application of advanced treatments [1-3]. Long term failure facilitates increased risk of infection and can lead to permanent disabilities or death. Current treatment methods include regular debridement of wounds, prophylactic antibiotics, special dressings, and wound drainage systems [1, 4]. Histopathologic testing of excised tissue from wounds for abnormal collagens, inflammatory cytokines, and phosphates have provided insight into the pathophysiology of wounds [1, 5, 6]. However, these are research techniques and due to their expense cannot be done with sufficient frequency to predict wound failure. We hypothesize that systems based on Raman and lifetime fluorescence imaging can give early warning of possible wound failure and provide additional information that will refine the treatment plan and improve wound healing prognoses.

    While all traumatic wounds express abnormal collagens in the first phase of the healing process, recent data suggests that these collagens dissipate throughout the later phases of normally healing wounds [1]. Conversely, failed wounds exhibit sustained, or increased abnormal collagen levels along with the presence of inflammatory cytokines [1]. An additional wound failure mechanism is the formation of Heterotopic Ossification (HO) [3, 7]. In these wounds collagen producing fibroblasts begin secreting phosphates which calcify quickly in the wound bed. If left untreated these constituents can coalesce into bone fragments causing pain in afflicted patients and often require deep debridement or amputation. Imaging systems based on both Raman and lifetime fluorescence technologies are both capable of detecting abnormal collagens and bone phosphates with high sensitivity and specificity while remaining robust to confounding factors that hinder *in vivo* imaging performance such as blood absorption and scattering. Previously these systems required point-by-point spectrometers with limited imaging capability and impractical illumination fluence.

2. **KEYWORDS:** Provide a brief list of keywords (limit to 20 words).
    - imaging
    - tumor
    - fluorescence
    - lifetime fluorescence

3. **OVERALL PROJECT SUMMARY:**

Fluorescence Lifetime imaging is a new imaging modality developed to overcome some of the limitations of standard, amplitude only spectroscopy. In standard fluorescence imaging the sample is pumped with a continuous wave (CW) laser source (typically UV) and the auto-fluorescence of the material is probed by detecting the longer wavelength emission of the sample (typically in the visible). This technique provides additional information over visible light imaging including biochemical composition, biochemical processes, etc. Additionally, dyes and fluorescent proteins can be introduced to the sample that bind to the molecules of interest with very high specificity and provide another data axis with which to identify composition. This technique has been used with great success in biological research but has not been as successful in medical imaging due to the incompatibility of some dyes with the human body, and low robustness to a clutter filled environment.

In contrast, lifetime fluorescence is a technique where the auto-fluorescence of a sample is probed in both the wavelength and time domains. This is accomplished by exciting the sample with a very short pulsed laser and detecting the auto-fluorescence to decay times at a range of wavelengths (Figure 1). Decay times are also dependent on the biochemical composition of the material and significant imaging contrast can be generated using maps of decay times. In many clutter dominated imaging fields, such as open/failed wounds, time resolved fluorescence is superior to amplitude only fluorescence because the fluorophore lifetime of a tissue is almost completely invariant to factors that would significantly degrade amplitude only measurements such as absorption by blood, scattering by tissue surface geometry, and other confounding factors.
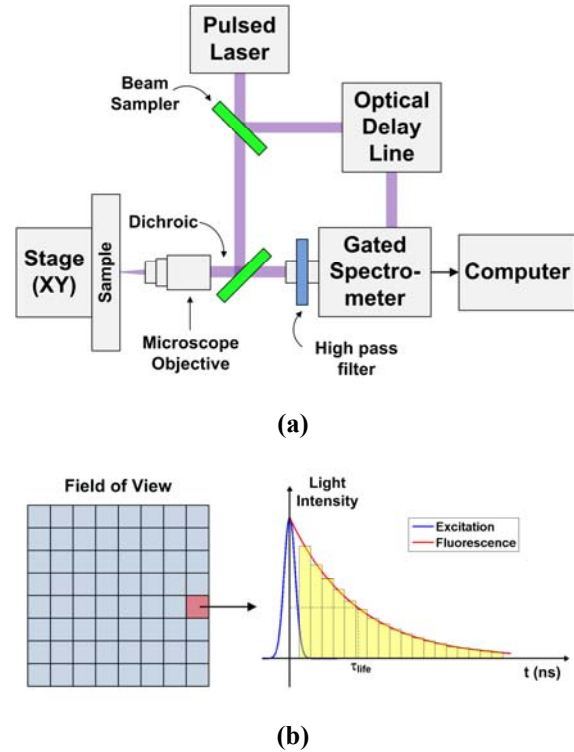


(a)

(b)

**Figure 1: Methodology of standard lifetime fluorescence imaging. (a) Block diagram of typical lifetime fluorescence imaging system with pulsed laser and translation stage, and gated detector. (b) Construction of an image from lifetime data. The fluorophore exponential lifetime at each pixel is determined.**

Lifetime Fluorescence has been applied to the detection of various forms of cancers including with sensitivities and specificities ranging from 80%-90%. Furthermore, systems based on lifetime fluorescence imaging have proven adept at identifying and delineating between various types of abnormal collagens that are present in the human body. However, current systems employing this technique use a computationally intensive method of lifetime extraction via orthogonal basis calculation (Laguerre polynomials) and curve fitting to identify fluorophore decay times and distributions (Figure 1b) [8-13]. Although very powerful, this technique generates far more information than is needed for contrast generation, is extremely slow and prone to significant error as the SNR drops. Furthermore, the inverse problem relating data to the fit is often ill-posed. There exists no robust, objective manner with which to choose the number of terms in expansion and different numbers of terms can all produce good fits

but provide completely different interpretations of the results. One major problem related to this computationally intensive data analysis is image acquisition phenomenology. Because the computation time per pixel is so long, most systems are based on a fiber probe phenomenology relegating the system to point spectroscopy. This requires mechanical scanning to create a 2D image which has hindered the clinical acceptance of this technique

While the challenges limiting clinical translation of FLIM are difficult to address, the potential sensitivity and specificity enabled by probing the unique optical properties of tissue through fluorophore lifetime based contrast generation presents a powerful capability for intraoperative detection and imaging of abnormal tissue. To take advantage of this contrast mechanism we developed a technique that seeks to generate contrast from differences in fluorophore lifetimes without the need to compute absolute lifetime values [14-17]. This relaxes the requirements on the temporal profile of the illumination pulse, enabling us to replace the picosecond pulsed laser with nanosecond pulsed light emitting diodes (LEDs) and forgo complex, computationally intensive data fitting routines thus representing a significant step towards clinical use.

This technique is called Dynamic optical Contrast Imaging (DOCI) and utilizes relatively long pulse widths (~ 30 ns) with short fall times (~ 1 ns) to produce contrast between fluorophores of difference decay rates. A pictorial representation of this concept is displayed in Figure 2(a) and additional details are discussed in section **Error! Reference source not found.**. A ~ 30 ns long pulse with ~ 1 ns rise and fall times illuminates the target with long 375 nm light. A gated intensified charge coupled device (iCCD) is oriented to detect the fluorescence emission. Two images are acquired: (1) A fluorescence emission is acquired in the middle of the pulse. The fluorescence lifetimes of most tissue constituents of interest in tumor imaging fall within the range of 1 ns to 10 ns [18-20]. An emission image, acquired starting at > 10 ns following initial illumination can be considered as an accurate representation of steady state tissue auto fluorescence. This image is labeled the calibration image. (2) An image is acquired starting at the decay of the illumination pulse. This image is labeled the decay image and upon acquisition the frame is normalized, pixel wise, by the calibration image and the resulting pixel values are proportional to the aggregate fluorophore decay time of the illuminated area. These pixel values represent 'relative' tissue lifetimes and are referred to as DOCI pixel values At its core, DOCI relies on the fact that the longer lifetime fluorphores produce signal than the shorter lifetime fluorophores when referenced to their steady state fluorescence.
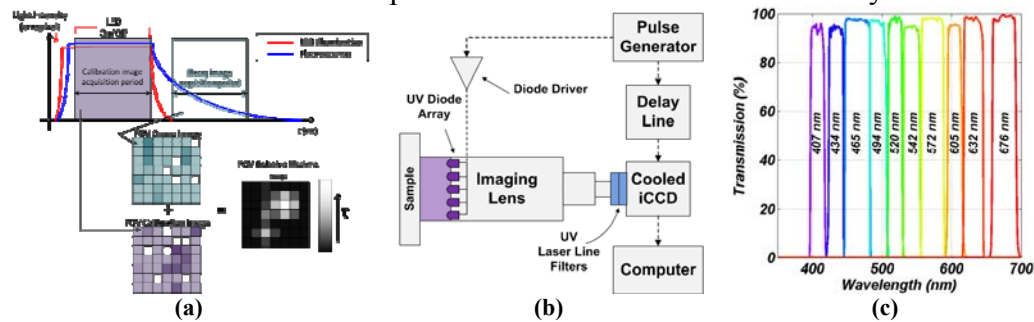


Figure 2: Novel Dynamic optical Contrast Imaging (DOCI). (a) Image generation algorithm. (b) Block diagram of system. (c) Laser line filter bank and associated wavelengths.

This approach has a number of key strengths that make it ideal for clinical imaging. First as discussed above, the lifetimes are not computed. Fitting is therefore not required, making the technique computationally simple. Second, since lifetime identification is not necessary, pulse widths and fall times can be relatively long (1-20 ns), thus opening the possibility of LEDs driven by electronic pulses. Third, the difference in signal between the emission decay of two fluorophores is positively correlated with gate time. In other words, the longer the gate is open during the decay image, the larger the difference signal. Additionally, the signal to noise ratio (SNR) increases significantly due to increases in signal and decreased measurement noise arising from the integrative properties of the sensor. This is in stark contrast to FLIM where gates need to be short to accurately sample the decay time.

A block diagram of our system architecture is shown in Figure 2(b) and consists of a cooled, intensified charged coupled device (CCD), UV (375 nm) diode array, pulse generator, and timing electronics. Candidate emission bands are displayed in Figure 2(c). Tissue relative lifetime values typically display a large variation with respect to emission wavelength and additional contrast and discriminatory power can be generated by analyzing the fluorescence emissions in specific bands [11, 12, 21].

Consider an illumination pulse modeled as an ideal rectangular pulse convolved with the impulse response of single pole low pass filter to model the band limit of the illumination pulse (Figure 3(a)). A single time constant exponential impulse response is described in **(1)** where $\tau k = \tau_d$ (illumination time constant), $\tau_1$ (fluorphore 1 time constant), or $\tau_2$ (fluorphore 2 time constant). This illumination profile is described in **(2)** where $T_0$ is the pulse width. The lifetimes of two distinct

$$h_k(t) = u(t)e^{-t/\tau_k} \quad (1)$$

$$x_d(t) = (\Pi_{T_0} * h_d)(t) \quad (2)$$

$$y_{1,2}(t) = (h_{1,2} * x_d)(t) \quad (3)$$

$$C_{1,2} = \frac{1}{T_1} \int_{-T_1}^{0} A_{1,2}y_{1,2}(t) + n(t) \quad (4)$$

$$D_{1,2} = \int_{0}^{T_2} A_{1,2}y_{1,2}(t) + n(t)dt \quad (5)$$

$$P_{1,2} = D_{1,2}/C_{1,2} \quad (6)$$

fluorophores can also be modeled with equation **(1)**. The fluorescence emission of the UV pumped fluorophores is written as the convolution of the diode illumination and fluorescence decay times (equation **(3)**). A graphical representation of these convolution integrals are shown in Figure 3(b) where the red and blue traces are the fluorescence emissions of fluorophores 1 and 2, respectively.

Here we bifurcate the treatment of basic description of DOCI to a noiseless (ideal) case detailed in the top row of Figure 3(c)-(d) and a noisy case in the bottom row of Figure 3 (c)-(d). As an added confounder we also consider that the pixels harboring the fluorphores of interest are subject to the effects of illumination/emission blocking obscurants chosen arbitrarily as 90% drop in detected fluorescence emission in fluorphore 1 and a 97.5% drop in fluorphore 2; the results of which are displayed in the top row of Figure 3(c). The noisy case also undergoes the same fluence absorption and then uncorrelated white measurement noise is added to the signal at an intensity to reduce the peak SNR of the received intensity of fluorophore 2 to 6 dB. Note that the time axes of Figure 3(b)-(d) are defined such that the illumination/emission decay occurs at t = 0;

A calibration measurement is acquired just before the illumination pulse begins to decay with a gate width of $T_1$. This process is described in equation **(4)** and displayed in Figure 3(c). The decay measurement undergoes similar acquisition methodology described by equation **(5)** and Figure 3(d) using gate width $T_2$. The resultant DOCI pixel value (equation **(6)**) is the ratio of the calibration and decay image and its value as a function of decay image gate width is displayed in Figure 3(e) where increasing the gate

length increases the difference signal computed between the two fluorophores and both signals converge (ideally) to the sum of the illumination and fluorophore decay times
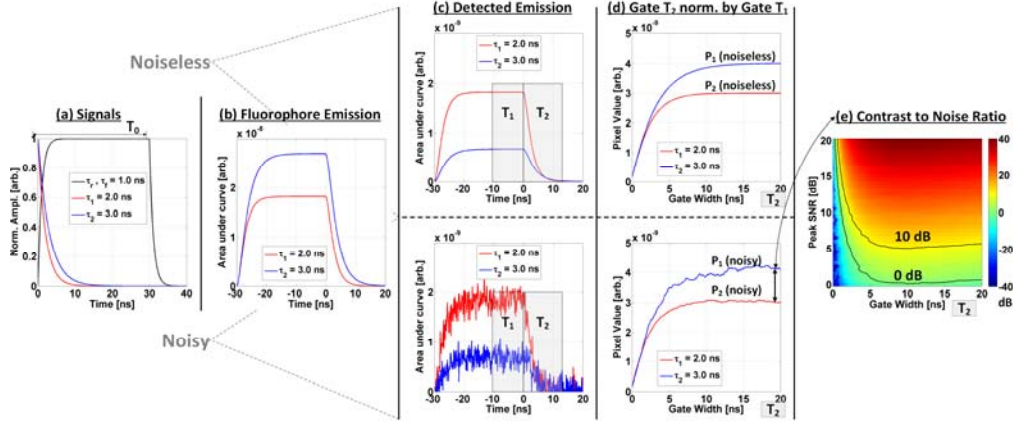


Figure 3: DOCI principles of operation. (a) Illumination profile and fluorphore lifetime profiles. (b) fluorophore emission computed by convolving the illumination profile with the fluorophore impulse response. (c) Random emission collection efficiency and measurement noise. (d) DOCI pixel value as a function of gate width. (e) Monte Carlo simulation of contrast to noise ratio.

The strength of DOCI is that it converts fluorophore lifetime into contrast by computing the area under the decay time curve normalized to the steady state fluorescence. In the limit of stationary noise this process is robust to variations in obscurants and can produce significant contrast under low SNR. Further, unlike standard FLIM, contrast is enhanced when the gate width is increased as it increases the overall number of collected photons while reducing noise variance.

A monte carlo simulation of the expected contrast to noise ratio (CNR) is displayed in Figure 3(f) as a function of gate width (x-axis) and peak SNR (y-axis). The contrast to noise ratio is defined as the difference signal SNR between the DOCI output of fluorphore 1 and fluorphore 2. The simulation results suggest that gated widths of 5 ns and longer are sufficient to achieve > 10 dB CNR when the peak emission SNR is > 6 dB and the fluorophore lifetimes are on the order of 1-3 ns. This data was used to define the gate width parameters of the system when obtaining the preliminary results.



Figure 4: Novel Dynamic optical Contrast Imaging (DOCI). (a) CAD design of large FOV system. (b) Assembled system used in ex vivo imaging study.

Our DOCI system implementation utilizes an illumination subsystem consisting of 6 UV-LEDs arranged in a circular formation (375nm, Thorlabs) each rated at 2 mW CW optical power. The LED circuit was driven by a pulse generator (AVR-E2-C, Avtech) at 50 volts with a current of ~1 Amp. The LED circuit operated at an average optical power of ~4.5 μW with peak power of ~ 1.5 W at a duty cycle of ~ 3e-6. A low duty cycle ensured thermal stability of the LED array and allowed the diode to produce peak optical powers many orders of magnitude above its rated CW power. The LED illumination characteristics (i.e. pulse width and peak intensity) were measured using a fast photomultiplier tube and confirmed to be linear with minimal ringing following the decay. An intensified CCD camera (DH 734 18U-03, iStar intensified CCD camera, Andor technology) captured images of the fluorescence calibration and decay images.

The gated, iCCD was operated with a gate width of ~ 5 ns and gate timing is controlled with a temporal resolution of 0.1 ps. The duration of the illumination pulse was ~ 30 ns (FWHM) with a repetition rate of 10 kHz. The pulse generator triggered the gated iCCD

to synchronize the optical illumination with the image acquisition. A motorized filter wheel (Edmund Optics, RS-232 Motorized Filter Wheel) containing ten bandpass filters (Semrock Fluorescence filters) centered at: 407nm, 434 nm, 465 nm, 494 nm, 520 nm, 542 nm, 572 nm, 605 nm, 652 nm, 676 nm with ~20 nm bandwidth (Figure 2(c)) was used to obtain spectral information. A UV rejection filter (Edmund Optics, 400 nm longpass filter) was used in conjunction with the bandpass filters to further reject reflected UV illumination. The fluorophore lifetimes of many tissue constituents (i.e. elastins and collagens) display a strong dependence on detection wavelength [14-17] thus some wavelengths may offer more discriminatory power than others. The optimal wavelength for detection of cancerous tissue *in vivo* is still unknown, thus the entire visible band was probed. To date, our data suggests that the 494 wavelength band is the most significant, but the others provide useful information as well. A CAD design of the DOCI system is shown in Figure 4(a) and a picture of the system installed in TPCL is in Figure 4(b)

The simplicity and intrinsic sensitivity of the technology enables real time imaging of large fields and is ideally suited to clinical imaging. Current image acquisition times take ~ 5 seconds and image processing time (currently performed offline with online processing planned for Aim 3) takes ~ 2 seconds, thus making this system highly clinically translatable.



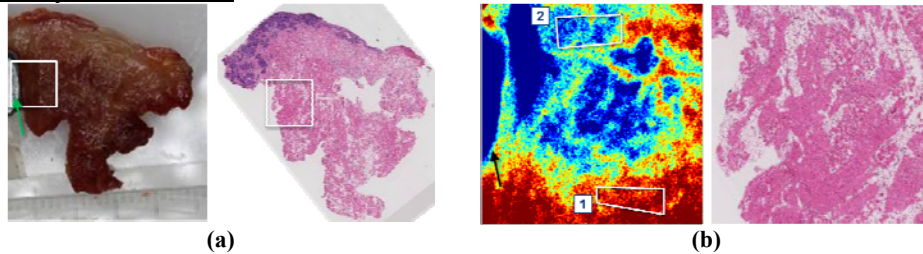(a)                                                                (b)

Figure 5: (a) Gross visible images (left column) and whole sample histology (right column). The white squares denote the 1 cm x 1 cm FOV acquired by the DOCI imaging system. (b) DOCI data with accompanying co-registered histologic section. Here, ROIs have been drawn by a physician blinded to the DOCI images and then superimposed upon the DOCI images and histology. Region 1 was fat and region 2 was tumor. The metallic fiducial marker is denoted with the green arrow in (a) and the black arrow in (b)

To evaluate the utility of the technique for in vivo imaging, a large trial of fresh ex vivo OSCC samples (45 patients, 88 individual samples) were imaged and the difference in relative lifetimes between areas of tumor, fat, muscle, and collagen were assessed. Regions of interest were drawn on the gross images (coregistered to DOCI images via the usage of an extrinsic fiducial marker) based on clinical visual assessment and histologic analysis. The results (sections 2.4 – 2.6) confirm the diagnostic power of the technique and provide strong support for transitioning the research into a clinical setting.

This study was approved by the University of California, Los Angeles (UCLA) Institutional Review Board (IRB). Patients undergoing surgical resection for OSCC were identified on a prospective basis. Prior to surgery, all patients signed written consent for involvement in the study. 45 patients were included in this pilot study. Following surgical resection, specimens were immediately sectioned into multiple fresh samples containing tumor and contiguous normal tissue. Calibration and decay images at the 10 wavelengths mentioned above were acquired with a metallic fiducial marker located at the edge of the field for registration with visible images. Visible images of the specimens were acquired with a digital SLR camera (Canon DSLR EOS Rebel T5i). After completion of imaging, specimens were subsequently fixed in 10% buffered formalin and processed to paraffin. Blocks were oriented with reference to the macroscopic images and DOCI maps to correlate imaging and histopathology. Visible images and registered H+E sections for an oral carcinoma resected from the tongue is displayed in Figure 5(a).

The resulting DOCI images were generated offline, following the acquisition of calibration and decay images, using the algorithms discussed in section **Error! Reference source not found.** and displayed in a false color map. Image registration was performed using the external fiducial marker clearly visible in both the DOCI and visible images. The DOCI image of the oral tongue tumor at 407 nm is displayed in Figure 5(b) where the longer lifetimes correspond to the red regions and shorter lifetimes correspond to the blue regions. The metallic fiducial does not exhibit detectable fluorescence when pumped at 375 nm and the resulting lack of signal is converted to a relative lifetime of 0 and displays blue in the false color map. Control points were selected on the visible image at locations corresponding to the edges of the external fiducial, and these points were used to create an affine transform: registering the DOCI images to the visible images by rotating, translating, and scaling the images. Following image generation, regions of interest (ROI) were drawn and recorded on the visible images corresponding to tissue types determined by assessing the tissues histologically. ROIs in the visible images were determined jointly by a head and neck surgeon and head and neck pathologist blinded to the DOCI images. The pixels on the DOCI images contained in the ROIs were then delineated and annotated (regions 1 and 2 in Figure 5(b)) then grouped by tissue type (tumor, collagen, fat, and muscle) and the mean relative fluorescence decay signature for all four tissue types was computed. Figure 6 depicts the work flow indicating image sets, hand delineated ROIs, and computation of relative lifetimes within the ROIs as a function of emission wavelength.

Two example tissue types from our trial are shown in Figure 5 and Figure 6 and demonstrate DOCI contrast across the FOV. Each visible image shows hand-delineated muscle, fat, tumor, and/or collagen ROIs. Corresponding histology is also shown highlighting quantitative differentiation among tissue types concordant with pathologic analysis. As observed in the images, tumor displayed decreased relative lifetimes when compared to muscle and fat across the filters utilized. Contrast between tissue types was evident across all the emission wavelengths. DOCI images using shorter wavelength emission filters where the tumor is depicted more blue in color (indicative of a shorter fluorescence decay) while the fat tissue appears red (indicative of a longer fluorescence decay).Imaging experiments were usually started ~ 45 minutes following surgical excision. Sample couriers typically required ~ 45 minutes to transfer samples from the OR to the laboratory. Although the optical properties of *ex vivo* specimens inevitably are altered due to changes in blood content and oxidation state of fluorophores, it has been shown that performing *ex vivo* fluorescence measurements on fresh specimens within the first few hours following resection can reliably reflect in vivo conditions [22].
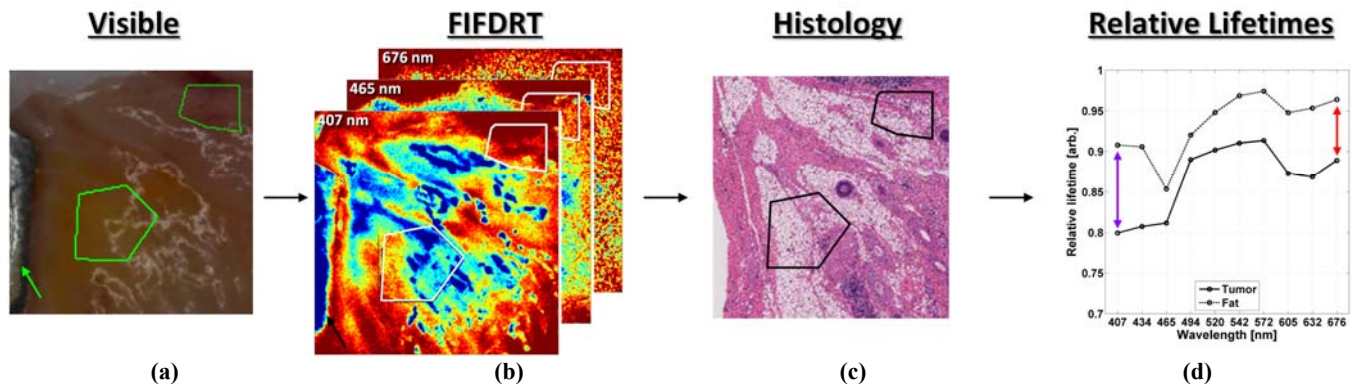


**Figure 6: Work flow using imaging data from a tumor resected from the floor of the mouth. (a) Tissue regions in the visible images are encircled using hand drawn ROIs provided by the physicians. (b) These ROI's are then superimposed on the DOCI images and relative lifetime values are extracted. (c) The regions of interest are then correlated with spatially registered histology and the tissue type annotated. (d) Statistical analysis is performed on the pooled DOCI data grouped by tissue type. The metallic fiducial marker is denoted with the green arrow in (a) and the black arrow in (b)**

The basis of neoplastic tissue contrast in DOCI is due in part to both biochemical and structural changes that occur that alter the emission properties of cancerous tissue. These include: changes in nuclear size, a higher nuclear to cytoplasmic ratio, increased microvascularization, degradation of stromal collagen, and changes in cellular metabolism resulting in altered concentrations of NADH and FAD.[23] For OSCC, it is reported that the main contributor to fluorescence emission is NADH.[23, 24]. With carcinogenesis, the contribution of NADH to fluorescence substantially rises. NADH has a short lifetime (~ 0.5ns for unbound and ~1ns for bound form) and results in an overall decrease in fluorescence lifetime in malignant tissue.[23-26] These findings are consistent with our results. A reduced DOCI pixel value indicates a more rapid decay of fluorescence signal (i.e., "decay image") indicating an overall shorter lifetime.

The local and global contrast in the DOCI images varied with increasing center wavelengths and the results from the statistical analysis revealed that shorter wavelengths offer increased discriminating power between tumor and fat, while the longer wavelengths produced increased
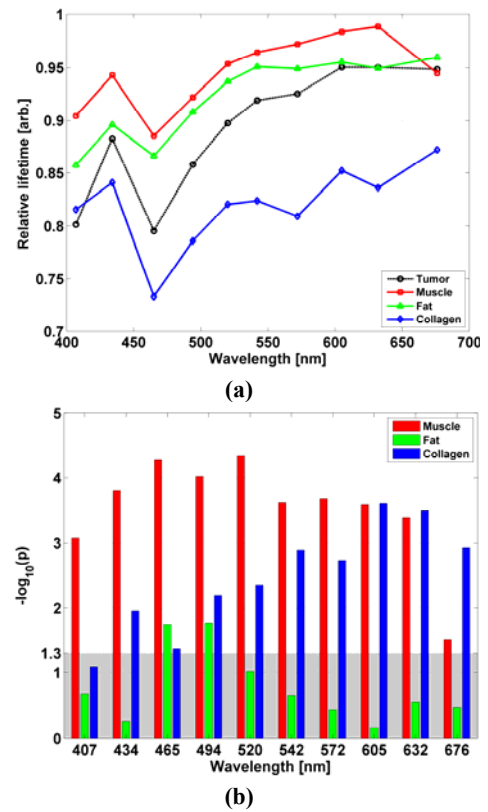


(a)



(b)

Figure 7: (a) Computation of relative lifetime for each tissue type as a function of wavelength. (b) Computation of p-values displayed as a Manhattan plot.

statistical significance in tests between tumor and collagen. However all wavelengths yielded statistically valuable information. The images of shorter -wavelength emission display higher image quality because the quantum efficiency of the iCCD camera used in this DOCI setup is highest in the 400 nm-500 nm band and is reduced in the 500 nm-600 nm. Photons of longer wavelengths have a low probability of absorption, therefore, images created by the CCD camera using these wavelengths are susceptible to decreased SNR and increased effects of noise aberrations, despite the fact that endogenous fluorophores in these wavelengths might be ideal for differentiation between normal and cancerous tissue.

The average relative lifetimes of different tissue types as a function of wavelength are shown in Figure 7(a). The difference in relative lifetime means within the ROIs was evaluated using a Wilcoxon rank-sum test; a modification of the t-test that does not require the two test populations to have equal variances and does not require normal distributions of sample population variance. A Kolmogorov–Smirnov test conducted on DOCI pixel sample pools suggested ROI means were normally distributed but we opted to use the Wilcoxon rank-sum test as it is more stringent and thus forms a lower limit on the statistical significance of the imaging results.

Wilcoxon rank-sum tests were performed between DOCI pixels paired with pixels from identified tumor, fat, and collagen areas at each emission wavelength for a total of 60 pairwise tests. p-values were computed for each pair and the results are plotted in Figure 7(b) in negative $\log_{10}$ scale where a $p < 0.05$ was labeled as significant. Figure 7(b) is displayed in the style of a Manhattan plot where smaller p-values (increased significance) are mapped to larger bars in the bar plot. Further the 0.05 threshold is denoted with the gray shaded area in Figure 7(b). All bars above the threshold are labeled significant.

The p-values for the tumor-muscle, tumor-fat, and tumor-collagen pairs are denoted with the red, green, and blue bars respectively. Significance was observed between tumor and collagen for all ten band-pass filters; between collagen and tumor in nine out of 10 filters; between fat and tumor in 2 of the 10 filters. In general, longer wavelength filters provided better quantitative contrast between tumor and collagen and shorter wavelength filters provided better contrast between tumor and fat muscle and collagen.

Recently, we have been able to configure our DOCI system for clinical use. A small pilot *in vivo* study was performed in OSCC patients. Images were taken of the tumors in vivo; then immediately afterwards images were acquired of the resected lesions.
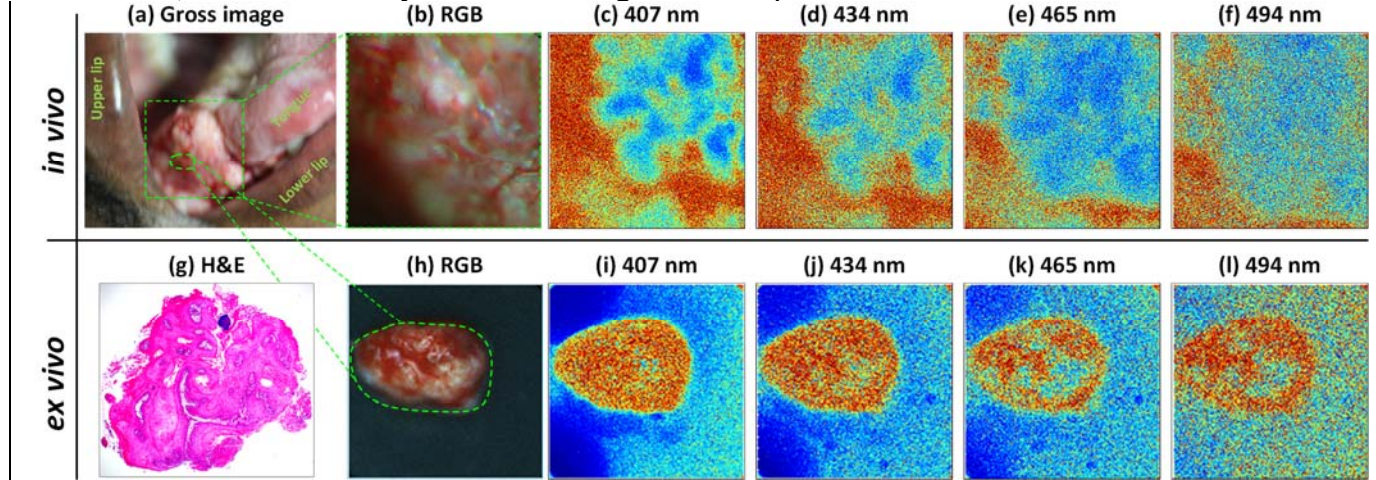


**Figure 8:** *In vivo* **imaging of tongue cancer. (a-b) visible image of cancer,(c-f) DOCI images at corresponding wavelengths (g) Histology (h) visible image of biopsy (i-l) DOCI images of biopsy.**

*in vivo* DOCI images of the mass shown in Figure 8(a),(b) are displayed in Figure 8(c)-(f) and reveal a cauliflower like structure typical of exophytic oral tongue carcinoma. The tumor areas demonstrated a reduced relative lifetime (DOCI pixel) to the surrounding tissue as was also observed in the *ex vivo* images. The DOCI images of the biopsied tissue (Figure 8(h)) are displayed in Figure 8(i)-(l) with limited contrast across the lateral extent of the tissue. H&E stains (Figure 8(g)) confirmed that the entirety of the biopsy was tumor, therefore limited contrast was expected in such a uniform field. The observed DOCI *in vivo* imaging and histological results correlate exactly with those seen in our ex vivo study. Due to this agreement in observed optical properties the methodologies analysis techniques optimized in the ex vivo trial are <u>directly translatable</u> to the proposed surgical study.

Biocompatible Raman imaging of tissue, particularly imaging of tissue *in vivo*, is difficult and has not yet translated to clinical settings. Most Raman techniques are time-consuming, require expensive and bulky systems, and are destructive in nature due to large illumination fluence [1–3]. There exist many disorders that cannot be detected or imaged via traditional methods and could use the high specificity that Raman signals offer. The detection of bone tissue that forms outside the skeleton is an ideal candidate disorder, as we found, by using the unique Raman signature of bone [1–4]. This mineralization growth occurs in traumatic wounds of the limbs where the injury affects soft tissue and is prevalent in combat wounds [5–8]. HO also arises in spinal injuries, severe burns and in the surgical beds resulting from orthopedic surgery complications [1,6,9,10]. The biochemical and physiologic mechanisms surrounding HO are not well understood and many precursors of HO are often poor predictors of the eventual establishment of HO, e.g. not all detectable fibrous abnormalities lead to

HO [5,8]. In failed wounds in the extremities (limbs), bone growth is impossible to detect in the early stages and treatment includes resection of the ossified (mineralized) areas and topical or intravenous delivery of medications. The delayed detection followed by late treatment can lead to amputation to avoid potentially life threatening infection [4]. While early detection is crucial, current technologies including X-ray (CT) and Magnetic Resonance Imaging (MRI), are limited and do not offer the resolution and specificity that is required in HO detection. Typical resolution limit for a CT scan is about 1 mm [11] however these scans are not practical for daily patient monitoring due to high costs and, most importantly, high levels of ionizing radiation [12]. There exist a need for improved imaging techniques capable of providing fast, inexpensive, *in vivo* compatible detection at a stage early enough to allow for appropriate treatment that reduces complications and costs and improves outcomes.

Traditional Raman detection involves point measurement and acquisition of Raman spectra using a spectrometer. Highly focused laser beam is illuminating the sample at each location and collects the Raman spectra until enough signal is collected. The spectra obtained from such an acquisition procedure are then compared to a known spectral database to find a match. These spectra can serve as a fingerprint to identify elements of a sample and, in the case of medical diagnostics, the constituents of tissue. In spectrometer based methodologies, detection is performed by raster scanning the sample area point by point and then various coloring techniques are used to create contrast maps corresponding to the spatial location of a particular constituents. This method is very specific however, it is a time-consuming processes that cannot be easily applied *in vivo* due to several limiting factors [13,14]. Two prominent problems are artifacts caused by the natural movements of the patients, and the high fluence levels of the illumination source. Moreover, this methodology does not scale efficiently into imaging large field of view of 0.1 cm$^2$ and above. In microscopic Raman imaging, a highly focused beam of a laser source can create an enormous power density of few Watts per cm$^2$, using a microscope objective lens, while scanning field of view is in the order of few dozen microns. Imaging *in vivo* human tissue cannot be exposed to high levels of fluence due to Maximum Permissible Exposure (MPE) limitations set by ANSI safety code [Z136.1-2007].

Since Raman scattering is an extremely weak phenomena, a powerful laser source, or alternately a highly focused beam, is required in order to generate a detectable signal. High fluence levels can cause dehydration of the tissue, denaturation of proteins, and destruction of other constituents. Another hurdle is overcoming the broad fluorescence signals that arise in tissue that often requires photo-bleaching or extremely complicated laser systems to generate a 'cleaner' Raman signal [15]. Stokes Raman signals are several order of magnitude weaker than fluorescence signals with the occurrence of about 1 in every 1 million photons. There exist several ways to amplify Raman signals, amongst them are stimulated themes such as Coherent Anti-stokes Raman Scattering (CARS) and Stimulated Raman Scattering (SRS) [16]. Clinical acceptance of these methods has not been proven due to the need for establishing a coherence illumination conditions and the requirement of expensive and bulky laser systems. These patient sampling and biocompatibility issues indicate that traditional Raman techniques, though of extreme utility in *in vitro* or *ex vivo* settings, are currently not practical for *in vivo* or translational research applications.

Monochromators display significant off-axis aberrations due primarily to the entrance slit, dispersive element within the instrument, and collimating optics. Thus images formed from radiation passing through the entrance slit have poor resolution and aberrations in the very center of the FOV and progressively worse to unusable image quality as one observes radialy outward from the center. This limits most

monochromator based systems to raster scanning only. In addition to significant off-axis aberrations, monochromators suffer from extremely low throughput on the order of - 30 dB. This is governed by the spectral resolution of the system. A narrow slit provides a larger solid angle of diffracted light which produces a broader spread of spectral components at the detector and thus higher spectral resolution. However, a narrow slit also reduces the available light at the detector thus resolution is only gained at the expense of signal and hence acquisition time. Furthermore, Raman signatures, such as the CH stretch are narrow $(1 - 10 \text{ cm}^{-1})$ and necessitates the use of a narrow entrance slit .
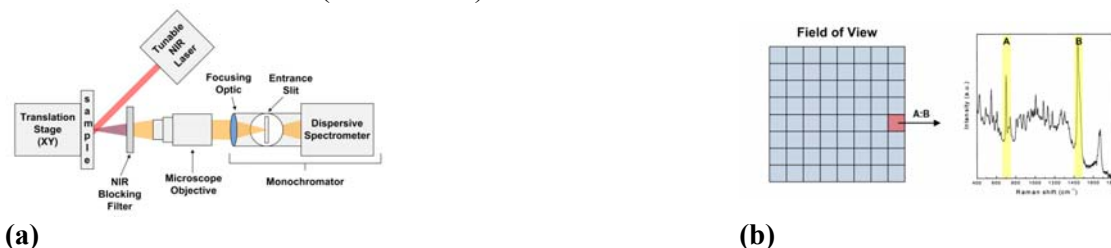
(a)

(b)

**Figure 9: Methodology of Raman spectroscopic imaging. a.) Block diagram of typical Raman spectroscopic imaging system with grating spectrometer and translation stage. b.) Construction of an image from Raman spectra using band area ratios. Most Raman imaging systems compare the power of one particular peak to a reference peak. A false color map is assigned to a range of ratios and then the ratio map is displayed as an image.**

One final point is the inefficiency of data use. Raman based imagers typically employ a band area ratio algorithm to generate images (Figure 9c). This equates to only a fraction of the total acquired spectrum utilized for image formation and represents a significant inefficiency in operation. The acquisition of unused data contributes significantly to impractically long acquisition times and is one of the primary hindrances to widespread clinical acceptance.

**UCLA system**

We have built the first Raman imaging system that acquires the full field in parallel by using tuned illumination and narrow band detection. A block diagram of this setup is displayed in Figure 10a. This architecture eliminates the monochromator and replaces it with a standard CCD focal plane array coupled to a very narrow, high throughput bandpass filter. The Raman imaging system tunes the illumination wavelength such that the expected Raman shifted wavelength (i.e. shifts for gliomas or HNSCC) falls into the filter pass band. Fast switching between wavelengths will allow high speed acquisition of the entire field of view for each shifted band of interest with extremely low illumination fluence.

**Results**

**Microscopic results**

To test the detection sensitivity and resolution of the system fragments of ground bone were sandwiched between layers of tissue analogues. A gray scale micrograph of the chosen fragment is displayed in Figure 10b where the bright spot is the bone fragment and the surrounding textured area is scotch tape. Scotch tape was selected as the mounting material because it has relatively good transmission at 611 nm and displays a low Raman emission at the 1090 cm-1 band. The bone fragment measures ~ 150 um in diameter and is ~ 10 um thick.

a.)                                    b.)                                    c.)
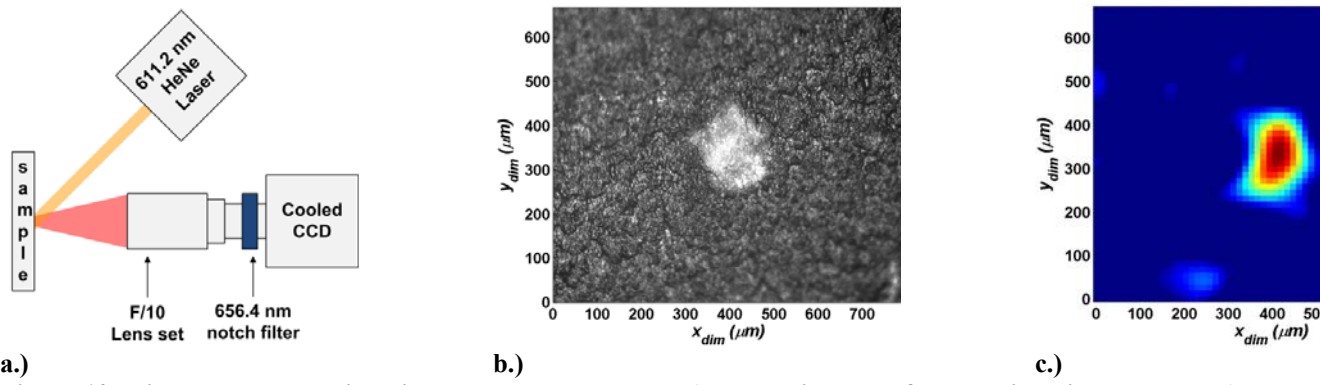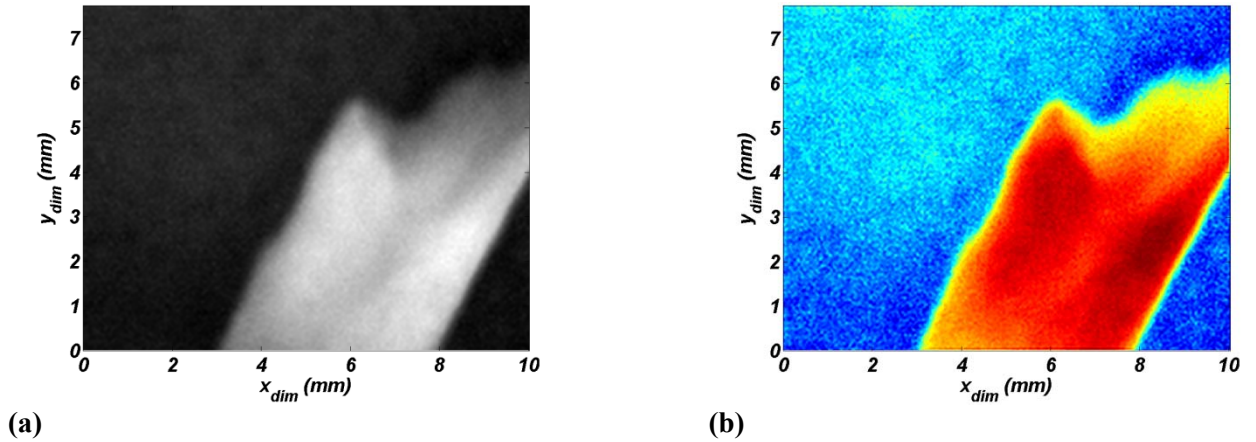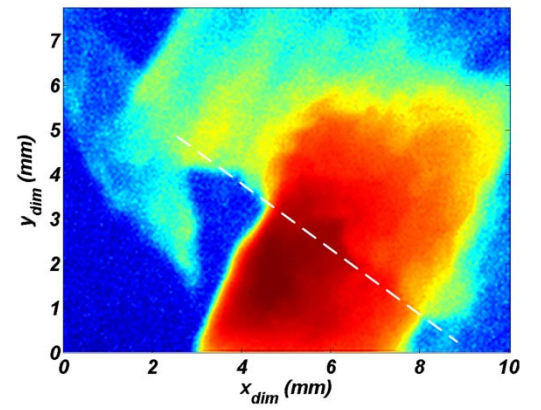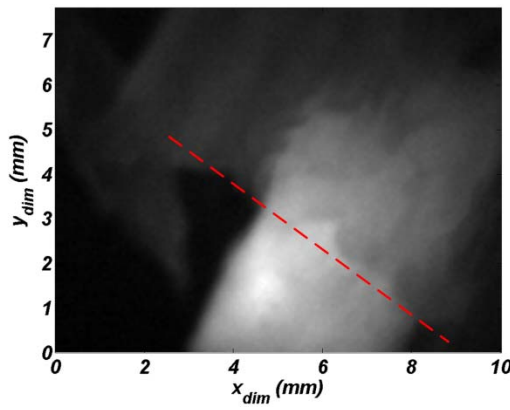
**Figure 10: Video rate Raman imaging system and results.  a.) Block diagram of Raman imaging system.  b.) graysc**
**of bone fragment on scotch tape.  c.) Raman image of Bone fragment.  Red corresponds to an increase in detected signa**

The full field of the Raman imaging system is displayed in Figure 10c where lighter shades of gray correspond to a higher level of received light at 657 nm (1090 cm-1 shift).The bone fragment is located at ~ 1 mm x 1 mm in the field and displays significant SNR.  The light areas located on the left side of the image are the Raman signature of the scotch tape.  Although clutter is visible in the image, the difference signal SNR between bone fragment and tape clutter is > 15 dB.  From the inset image a total of 12 x 12 = 144 pixels were determined to lie within the boundaries of the target.  This confirms that the Raman imaging system is limited by systemic parameters such as scattering coefficient, optics, and CCD/CMOS spatial sampling frequency and not by some intrinsic physical limit as are X-ray and MRI.  From this data, a back projected pixel size (on target) of ~ 25 μm was computed; ~ 6x the resolution available to clinically deployed X-ray imaging systems.  This is larger than the diffraction limited spot size of the system optics and confirms that our resolution is currently limited only by physical optics.

**Wide field results**

Following the resolution characterization, experiments were performed to determine system performance over a wide field of view and assess light scattering and absorption due to overlying muscle tissue.  A bone chip measuring 2 mm x 8 mm from the same donor bone as the previous sample was selected and placed on the scotch tape backing used in the bone fragment experiments.  The imaging system optics were then modified and the field of view expanded from 0.7 mm x 0.8 mm  to ~ 7 mm x 8 mm.  The illumination beam total power was limited to ~ 2 mW and with a ~ 1 cm diameter beam. This corresponds to ~ 25 μW/mm$^2$ and is orders of magnitude less than the accepted ANSI standards.





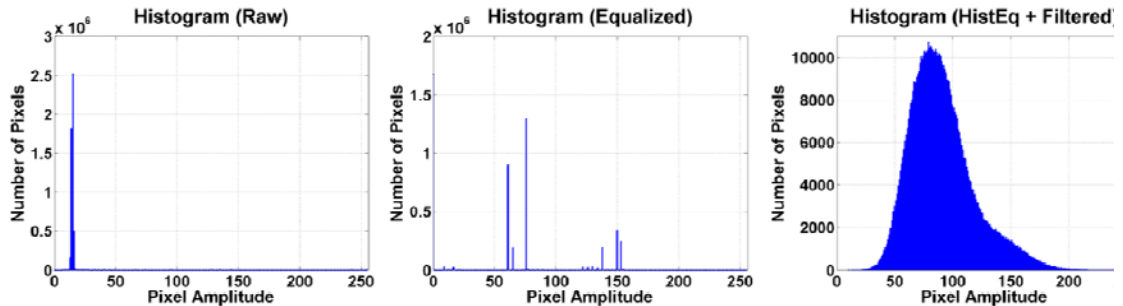(a)                                                    (b)

**(c)** **(d)**

**Figure 11: Wide field Raman imaging of bone. (a) Grayscale of exposed bone chip. (b) False color image of exposed bone chip. (c) Grayscale of bone chip obscured by 2 mm of muscle tissue. (d) False color of bone chip obscured by 2 mm of muscle tissue.**

A grey scale image of the bone chip after a 5 minute exposure is displayed in Figure 11a and reflect the level of detected light at 657 nm emitted by the 1090 cm-1 shift. The false color mapping of this image is displayed in Figure 11b where red corresponds to higher intensity and blue lower. Edge definition is excellent and noise limited contrast is > 20 dB. A grayscale Raman image of the same bone chip with the top half obscured by ~ 1 mm thick muscle tissue is displayed in Figure 11c and false color map in Figure 11d. The muscle tissue covered the area in the image northeast of the dotted line. Light throughput is still sufficiently high for high contrast imaging with signal SNR still > 20 dB. While edge definition has suffer slightly from the diffuse scattering of the emitted 657 nm light through the overlying tissue this intensity map still displays contrast sufficient for calcification detection.

**Image processing**

Contrast enhancement and CCD readout noise suppression algorithms have been developed to extract the maximum contrast from each scene. The algorithms devloped to extract the contrast observed in Figure 10 and Figure 11 are discussed below.

Image processing was done with MATLAB's histogram equalization and 2D spatial convolution functions. The Raman scatter light is > 6 orders of magnitude below the applied illumination power and algorithms that convert low signal to useful contrast are imperative to the development of a clinical system. The dim raw images generated by Raman imaging system typically have a significant number of pixels in the lower intensity regions of the intensity scale. The first step in the enhancement process is histogram equalization which spreads the distribution of the pixel intensities such that the cover the entire range afforded by the display system. This is achieved through a non-linear (sigmoidal) mapping of pixel values. While this brings out the features from the image, it accentuates high frequency noise. To decrease noise in the image, a 2D finite impulse response filter designed in the spatial frequency domain with the FFT was created to minimize enhancement noise while maintaining edge definition.

**Figure 12: Implementation of histogram equalization and low-pass filtering a.) Histogram of the raw image. (b) histogram after equalization. (c) histogram following low-pass filter.**

Figure 12a displays the pixel intensity histogram of a typical raw Raman image. A significant majority of the pixels display values in the lower 10% of the visible range. Histogram equalization intelligently redistributes these values such that they enhance contrast (Figure 12b). However, this process gives rise to high frequency noise as is evidence by the discrete nature of the histogram. Figure 12c displays the histogram of the final processed image following low pass filtering where the distribution of pixels has been smoothed out thus reducing high frequency noise.

Our proof of concept macro-imaging Raman system is adapted to acquire full field images of tissue in real time without resolving Raman spectra, to capture the location of bone tissue structures (Figure 1). By using the unique Raman stokes signature of the Phosphate ($PO_4^{3-}$), specifically the tetrahedral symmetric stretching of the P-O bonds [1–4], a successful detection of the inorganic constituent within the bone structure is possible. Phosphate is a major building block of hydroxyapatite, the calcium mineral found in bone and heterotopic ossification, and is not found in significant quantities in other tissues. This signal exhibit a very strong signal that can overcome the broad fluorescence background found in bone and flesh, and ultimately can enable *in vivo* detection.
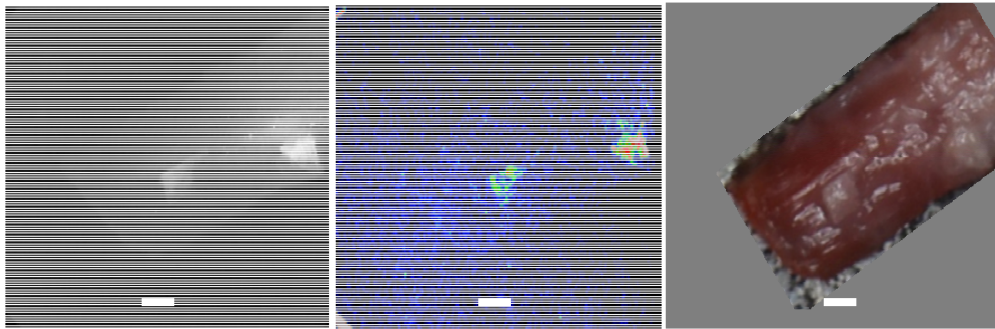


Fig. 1. Bone on tissue imaging. Right: Color image taken after the experiment showing the tissue sample with 2 pieces of bone on top. Adipose tissue and cortical bone fragments were taken from bovine samples. Left: Grey scale image of the fluorescence and Raman signals at optical wavelength of 852nm (excitation wavelength is at 785 nm), showing both the bone and the soft tissue fluorescence signals. Middle: Raman signal computed image showing the bone locations. The muscle tissue fluorescence signal reduced significantly and showing close to background signal level. Bone signal is measured at about x10 larger than the surrounding tissue, which translate to 20dB in Signal to Noise Ratio (SNR). Image threshold has been applied, due to laser beam non-uniformity signal levels from the two bone pieces at the two locations locations are different. Scale bars in all images is 1 mm.

Further experiments conducted with collaboration of the dental school, enabled validation of the imaging results using a microCT scanner (figures 2, 3). This has enabled us to show proof of concept imaging approach on detection of bone on the surface and also under a layer of tissue.
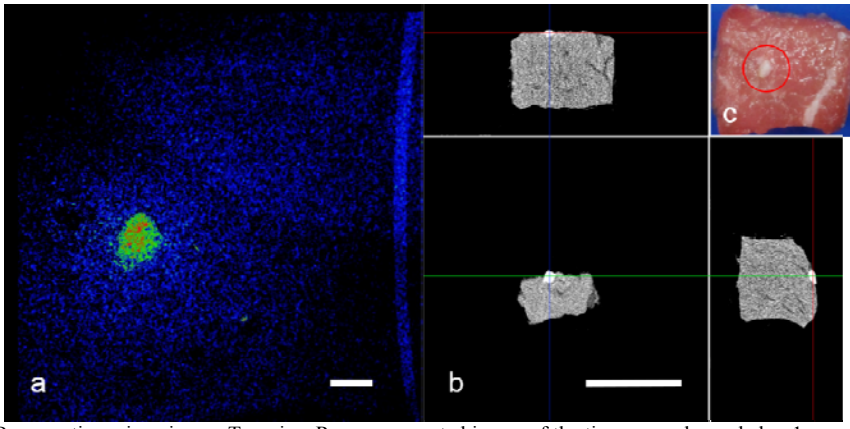
Fig. 2. Bone on tissue imaging: a. Top view Raman computed image of the tissue sample, scale bar 1 mm. b. microCT projections of the sample, top and perpendicular side views, scale bar 1 cm. c. Top view color image with bone fragment encircled in red, bone size is ~1 mm.
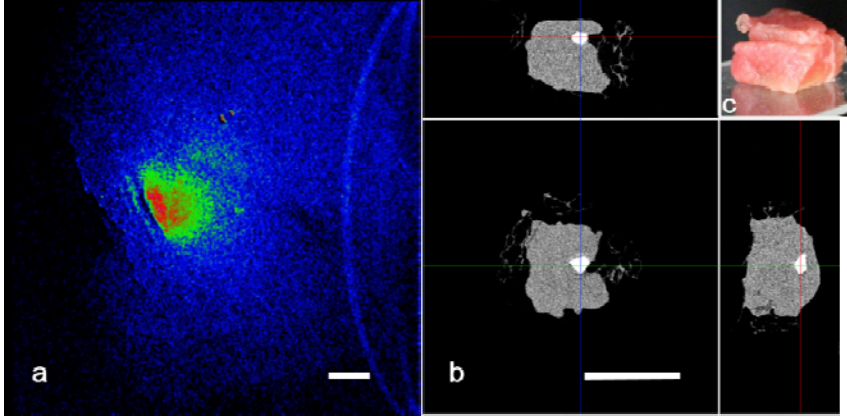


Fig. 3. Bone embedded in tissue: a. Raman computed image of the tissue sample, the bone (~1 mm in size) Raman signal scattered through the top layer showing diffused boundaries and effectively lowering resolution, scale bar 1 mm. b. microCT projections of the sample, top and perpendicular side views, scale bar 1 cm. c. Angled side view color image, showing top layer of meat (~2 - 3 mm thickness), and a bottom piece (~8 mm).

The system was built around an 852 nm tunable narrow-band optical filter (Semrock, LL01-852-25) mounted in front of the imaging optics and serves as the Raman band differentiator (figure 4). The rest of the system comprises of a 1 mega-pixel intensified CCD (ICCD) camera (Andor, iStar 334T), macro lens (Canon, MP-E 65mm), 90mW 785 nm diode laser (Thorlabs, L785P090), and additional optical filters to block light that falls outside the detection band: 785 nm notch filter (Semrock, NF03-785E-25), and a bandpass filter at 842 nm (Semrock, FF01-842/56-25) central wavelength with 30 nm spectral bandwidth (full-width half-maximum). The laser beam was defocused using an aspheric lens (Thorlabs, C280TME-B) and offered illumination area of 30 mm$^2$ at power density of 250 mW/cm$^2$, well below the MPE.
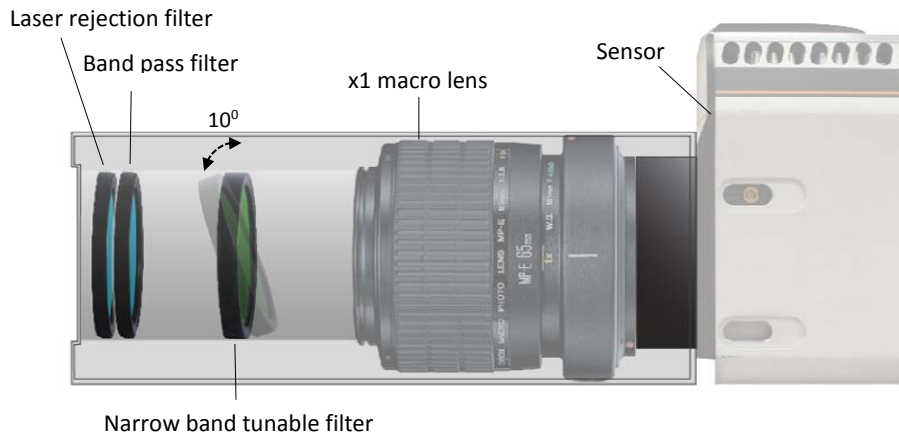
Fig. 4. Imaging system schematics: Intensified CCD camera sensor records 1 cm field of view images of a single wavelength band through set of optical filters. The tunable Raman filter in the heart of the system transmits 849 nm emission at 10 degrees pivot rotation and 852 nm emission at 0 degrees – perpendicular to the optical axes. Front filters include 785 nm laser rejection filter and a band pass filter reducing broad fluorescence signals. This compact imaging setup utilizes off the shelf parts: Macro lens, optical filters and a near infra-red sensor.

The narrow band optical filter enables sensitive selection of the incoming signal from 849 to 852 nm. Tuning the narrow-band filter is done by changing the angle in which it is positioned in relation to the optical axis. Through angular adjustment, a wavelength selection of the incoming image is achieved, and offers multi spectral selection for each recorded image: 852 nm central wavelength at 0 degrees, to 849 nm at 10 degrees rotation. This is a common method in which thin-film optical filters are tuned for specific wavelength. The final Raman map is computed by subtraction of two images: First image captures the unique Raman stokes signal of the phosphate symmetric stretch at 960 cm$^{-1}$ (849 nm), and the second image captures only fluorescence and background signals of the tissue at 1002 cm$^{-1}$ (852 nm). The two images, each at different wavelength, hold sufficient information to localize the unique Raman signatures of bone. By image subtraction of the 849 nm image and the 852 nm image using ImageJ, a composite image set showing only the bone's Raman signal is composed. The new image shows a 2D representation of bone locations by the difference between the two wavelength selections.

The adipose tissue and cortical bone selected for this experiment were taken from a food-grade bovine sample. No Institutional Review Board approval was required. 1 mm bone segments were chosen since this is approximately the detection size limit (slice width) of medical x-ray (CT) systems.

The x-ray scan were taken by a high-resolution microCT (SkyScan 1172, Bruker MicroCT N.V., Kontich, Belgium) at an image resolution of 27.4 μm (70 kV and 141 μA radiation source, using a 0.5mm aluminum filter), and imaged using DataViewer software provided by the manufacturer. Raman acquisition in figures 2 and 3, were captured using a near infra-red CCD camera (Andor, iKon-M 934) as means to compare performance of the two systems. This camera has acquired higher resolution images however at the cost of longer exposure times due to lack of signal amplification that is available with the ICCD.

4. **KEY RESEARCH ACCOMPLISHMENTS:**
   - Development of DOCI imaging technology
   - Development of DOCI algorithm
   - Design, construction, and verification of DOCI imaging systems
   - Large tumor tissue data set collection

5. **CONCLUSION:**
   Significant work has been achieved in imaging and detection of tissue constituents correlated with failed wounds. We intend to continue this work with extensive preclinical animal imaging

6. **PUBLICATIONS, ABSTRACTS, AND PRESENTATIONS:**

a. List all manuscripts submitted for publication during the period covered by this report resulting from this project. Include those in the categories of lay press, peer-reviewed scientific journals, invited articles, and abstracts. Each entry shall include the author(s),

article title, journal name, book title, editors(s), publisher, volume number, page number(s), date, DOI, PMID, and/or ISBN.

1. Lay Press:

2. Peer-Reviewed Scientific Journals:

   a. A. Papour, Z. Taylor, A. Sherman, D. Sanchez, G. Lucey, L. Liau, O. Stafsudd, W. Yong, W. Grundfest, "Optical imaging for brain tissue characterization using relative fluorescence lifetime imaging," J. Biomed. Opt., vol. 18, no. 6, pp. 060504, Jun 2013; doi: 10.1117/1.JBO.18.6.060504

   b. A. Papour, Z. Taylor, O. Stafsudd, W. Grundfest, I. Tsui, "Imaging autofluorescence temporal signatures of the human ocular fundus in vivo," Journal of Biomedical Optics, submitted 2015.

   c. A. Papour, J. H. Kwak, Z. Taylor, B. Wu, O. Stafsudd, W. Grundfest "Raman imaging for bone growth in flesh sans spectroscopy," Biomed. Opt. Ex., submitted 2015.

   d.

3. Invited Articles:

4. Abstracts:

b. List presentations made during the last year (international, national, local societies, military meetings, etc.). Use an asterisk (*) if presentation produced a manuscript.

   1. "Rapid optical imaging for brain tissue characterization and biobanking using contrast based spectro-temporal autofluorescence signatures," Society for Brain Mapping and Therapeutics conference, LA 2015.

   2. *"Real time early detection imaging system of failed wounds and heterotopic ossification using unique Raman signatures," SPIE Medical Imaging, Orlando 2015.

   3.

7. **INVENTIONS, PATENTS AND LICENSES:** List all patents and licenses applied for and/or issued. Each entry must include the inventor(s), invention title, patent application number, filing date, patent number if issued, patent issued date, national, or international.

   a. W. S. Grundfest, O. M. Stafsudd, P.-C. Jiang, A. Papour, and Z. D. Taylor, "System and method for time-resolved fluorescence imaging and pulse shaping," Pending WO2013131062 A106 Sep. 2013.

   b.

8. **REPORTABLE OUTCOMES:**
   See above

9. **OTHER ACHIEVEMENTS:**

   "Nothing to report."

## 10. REFERENCES:

[1]     N. J. Crane, T. S. Brown, K. N. Evans, J. S. Hawksworth, S. Hussey, D. K. Tadaki, and E. A. Elster, "Monitoring the healing of combat wounds using Raman spectroscopic mapping," *Wound Repair and Regeneration,* vol. 18, pp. 409-416, 2010.

[2]     A. Medina, P. G. Scott, A. Ghahary, and E. E. Tredget, "Pathophysiology of Chronic Nonhealing Wounds," *Journal of Burn Care & Research,* vol. 26, pp. 306-319, 2005.

[3]     B. K. Potter, T. C. Burns, A. P. Lacap, R. R. Granville, and D. A. Gajewski, "Heterotopic Ossification Following Traumatic and Combat-Related Amputations," *Journal Of Bone & Joint Surgery,* vol. 89a, 2007.

[4]     P. G. Bowler, "Wound pathophysiology, infection and therapeutic options," *Ann Med,* vol. Vol. 34, pp. 419-427, 202.

[5]     M. C. Robson, "Disturbances of Wound Healing," *Annals of Emergency Medicine,* vol. 17, pp. 1274 - 1278, 1988.

[6]     J. Li, J. Chen, and R. Kirsner, "Pathophysiology of acute wound healing," *Clinics in Dermatology,* vol. 25, pp. 9–18, 2007.

[7]     D. E. Garland, C. E. Blum, and R. L. Waters, "Periarticular Heterotopic Ossification in Head-Injured Adults," *J Bone Joint Surg Am.,* vol. 62-A, pp. 1143-1146, 1980.

[8]     L. Marcu, J. A. Jo, P. V. Butte, W. H. Yong, B. K. Pikul, K. L. Black, and R. C. Thompson, "Fluorescence Lifetime Spectroscopy of Glioblastoma Multiforme¶," *Photochemistry and Photobiology,* vol. 80, pp. 98-103, 2004.

[9]     P. V. Butte, A. N. Mamelak, M. Nuno, S. I. Bannykh, K. L. Black, and L. Marcu, "Fluorescence lifetime spectroscopy for guided therapy of brain tumors," *NeuroImage,* vol. 54, pp. S125-S135, 2011.

[10]    P. V. Butte, B. K. Pikul, A. Hever, W. H. Yong, K. L. Black, and L. Marcu, "Diagnosis of meningioma by time-resolved fluorescence spectroscopy," *Journal of Biomedical Optics,* vol. 10, pp. 064026-9, 2005.

[11]    Q. Fang, T. Papaioannou, J. A. Jo, R. Vaitha, K. Shastry, and L. Marcu, "Time-domain laser-induced fluorescence spectroscopy apparatus for clinical diagnostics," vol. 75, pp. 151-162, 2004.

[12]    J. D. Meier, H. Xie, Y. Sun, Y. Sun, N. Hatami, B. Poirier, L. Marcu, and D. G. Farwell, "Time-resolved laser-induced fluorescence spectroscopy as a diagnostic instrument in head and neck carcinoma," *Otolaryngology - Head and Neck Surgery,* vol. 142, pp. 838-844, 2010.

[13]    L. Marcu, "Fluorescence lifetime in cardiovascular diagnostics," *Journal of Biomedical Optics,* vol. 15, pp. 011106-10, 2010.

[14]    A. J. Sherman, A. Papour, W. S. Grundfest, Z. D. Taylor, and O. M. Stafsudd, "Normalized fluorescence lifetime imaging for tumor identification and margin delineation," in *SPIE Advanced Biomedical and Clinical Diagnostic Systems XI*, San Francisco, 2013.

[15]    Z. D. Taylor, A. Papour, O. M. Stafsudd, and W. S. Grundfest, Eds., *Lasers in Medicine* (Medical Devices. Wiley, 2012, p.^pp. Pages.

[16]    W. S. Grundfest, O. M. Stafsudd, P.-C. Jiang, A. Papour, and Z. D. Taylor, "Time-Resolved Fluorescence Imaging without Lifetime Fitting and Illumination Pulsed Shaping for Fluorescence Lifetime Imaging Microscopy (Film) Enhancement," United States of America Patent 61/605844, 2012.

[17]    A. Papour, Z. D. Taylor, W. Yong, M. S. John, O. Stafsudd, and W. S. Grundfest, "Multi-Spectral Fluorescence Lifetime Contrast Imaging for Brain Cancer Detection," in *Biomedical Engineering Society (BMES) Annual Meeting*, Atlanta, GA, 2012.

[18]    R. Cubeddu, G. Canti, A. Pifferi, P. Taroni, and G. Valentini, "Fluorescence Lifetime Imaging of Experimental Tumors in Hematoporphyrin Derivative-Sensitized Mice," *Photochemistry and Photobiology,* vol. 66, pp. 229-236, 1997.

[19]    P. Provenzano, K. Eliceiri, and P. Keely, "Multiphoton microscopy and fluorescence lifetime imaging microscopy (FLIM) to monitor metastasis and the tumor microenvironment," *Clinical & Experimental Metastasis,* vol. 26, pp. 357-370, 2009/04/01 2009.

[20]    P. S. Considine, "Effects of Coherence on Imaging Systems," *Journal of the Optical Society of America,* vol. 56, pp. 1001-1007, 1966/08/01 1966.

[21]    D. R. Collingridge, W. K. Young, B. Vojnovic, P. Wardman, E. M. Lynch, S. A. Hill, and D. J. Chaplin, "Measurement of Tumor Oxygenation: A Comparison between Polarographic Needle Electrodes and a Time-Resolved Luminescence-Based Optical Sensor," *Radiation Research,* vol. 147, pp. 329-334, 1997/03/01 1997.

[22]    G. M. Palmer, C. L. Marshek, K. M. Vrotsos, and N. Ramanujam, "Optimal methods for fluorescence and diffuse reflectance measurements of tissue biopsy samples," *Lasers Surg Med,* vol. 30, pp. 191-200, 2002.

[23]    R. A. Schwarz, W. Gao, C. Redden Weber, C. Kurachi, J. J. Lee, A. K. El-Naggar, R. Richards-Kortum, and A. M. Gillenwater, "Noninvasive evaluation of oral lesions using depth-sensitive optical spectroscopy," *Cancer,* vol. 115, pp. 1669-79, Apr 15 2009.

[24]    M. C. Skala, K. M. Riching, A. Gendron-Fitzpatrick, J. Eickhoff, K. W. Eliceiri, J. G. White, and N. Ramanujam, "In vivo multiphoton microscopy of NADH and FAD redox states, fluorescence lifetimes, and cellular morphology in precancerous epithelia," *Proc Natl Acad Sci U S A,* vol. 104, pp. 19494-9, Dec 4 2007.

[25]    D. C. De Veld, M. J. Witjes, H. J. Sterenborg, and J. L. Roodenburg, "The status of in vivo autofluorescence spectroscopy and imaging for oral oncology," *Oral Oncol,* vol. 41, pp. 117-31, Feb 2005.

[26]    Y. Sun, J. E. Phipps, J. Meier, N. Hatami, B. Poirier, D. S. Elson, D. G. Farwell, and L. Marcu, "Endoscopic fluorescence lifetime imaging for in vivo intraoperative diagnosis of oral carcinoma," *Microsc Microanal,* vol. 19, pp. 791-8, Aug 2013.